

Article

Sintering of Cermets: A Case Study of Sintering Ni–Co Ferrite with Ag-, Cu- and Ni-Dispersed Alloy Particles

Vera Lúcia Othéro de Brito ^{1,2,*} , Mônica Sumie Hieda ^{1,2}, Eduardo de Oliveira Silva Júnior ¹, Jessica Aparecida Nascimento Ferreira ¹ and João Paulo Barros Machado ³

¹ Instituto de Estudos Avançados, São José dos Campos 12228-001, Brazil; msumiehieda@gmail.com (M.S.H.); edu_oliveira_junior@hotmail.com (E.d.O.S.J.); jessicaanferreira@gmail.com (J.A.N.F.)

² Instituto Tecnológico de Aeronáutica—Programa de Pós-Graduação em Ciências e Tecnologias Espaciais, São José dos Campos 12228-900, Brazil

³ Instituto Nacional de Pesquisas Espaciais, São José dos Campos 12227-010, Brazil; joapaulo@las.inpe.br

* Correspondence: vlobrito@ieav.cta.br

Received: 4 March 2019; Accepted: 15 March 2019; Published: 20 March 2019



Abstract: Literature has shown that the development of ferrite cermets makes possible the enhancement of the mechanical properties of these ceramics for applications in electronics, magnetomechanical sensors, and inert anodes. In this work, a Ni–Co ferrite powder was mixed with metallic powders, compacted, and sintered. The metallic powders used were Ag–Ni and Cu–Ni, prepared by mechanical alloying, and commercial Ag and Ag–Cu powders. The microstructures, crystal structures, and chemical compositions of the sintered samples were analyzed. The Cu–Ni cermet did not present traces of second phases in its XRD pattern, and the experimental results indicate a high reactivity between the ferrite and the Cu–Ni alloy. In the Ag–Cu and Ag–Ni cermets, the composition of the metallic particles was nearly 100% Ag after sintering. It was observed that, for the production of ferrite particulate cermets, the composition, particle size, and melting point of the metallic phase must be carefully adjusted in order to obtain a material with proper chemical composition and microstructure (uniform distribution of the metallic phase and no cracks in the metal–ceramic interfaces).

Keywords: ferrites; cermets; mechanical alloying; magnetic ceramics

1. Introduction

Cermets are metal–ceramic composites that may have either a ceramic matrix or a metallic matrix. Some applications of ceramic-matrix composites are in tools, dies, seals, emitter cathodes, ignition pellets, and armor [1]. There are several synthesis methods for the production of ceramic-matrix cermets and they may be either reactive or nonreactive.

Ferrites are magnetic ceramics that have many applications in electronics, including magnetic [2,3], magnetoelectric [4] and magnetomechanical sensors [5,6]. Spinel ferrites are oxides that have a cubic crystal structure, where the oxygen anions form a face-centered cubic (FCC) lattice. The stoichiometry of a spinel ferrite is $(D_{1-\delta}T_{\delta})[D_{\delta}T_{2-\delta}]O_4$, where D is a divalent cation; T is a trivalent cation; parentheses represent the tetrahedral interstitial sites; brackets represent the octahedral interstitial sites; and δ is the degree of inversion.

Among spinel ferrites, the ones of cobalt-based composition retain the highest magnetostriction levels, which make them promising candidates for applications in magnetomechanical and magnetoelectric sensors [7,8]. Some works report the application of Ni ferrites in inert anodes for use in the industrial production of aluminum [9,10] as well as their interesting magnetostrictive properties

for sensor applications [11,12]. However, for some applications in magnetomechanical sensors, the material must have adequate mechanical strength, which requires strict control of the microstructure.

Some works in the literature recommend the use of cermet technology to increase the mechanical strength of ferrites used in magnetomechanical transducers. These works suggest the addition of Ag-based alloy particles to the ferrite so as to produce a particulate cermet with good mechanical properties and high magnetoelastic sensitivity [13,14]. The study of techniques to adjust the microstructure of ferrites, aiming for the enhancement of mechanical strength, is important not only for the development of ferrite magnetomechanical transducers but also for the development of surface-mounted devices (SMDs) such as inductors and transformer cores [15].

The metal–ferrite interaction at high temperatures has been studied by several authors in works about brazing and soldering of electronic and electrochemical components and devices, such as chip inductors, magnetic recording heads, gas sensors, and other applications [16–21]. Many aspects of this interaction have been assessed, such as wetting of ferrites by metals in liquid state and adhesion between the metal and the ferrite. However, very few articles deal with the production of ferrite-matrix particulate cermets for electronics; most of them deal with applications of the material in inert anodes [22–25].

The purpose of this work is to evaluate the metal–ceramic interaction during sintering of a particulate cermet composed of a Ni–Co ferrite matrix and Cu–Ni, Ag–Cu, Ag–Ni, and Ag as metallic particles.

2. Materials and Methods

Ceramic-matrix cermet samples were produced using particulate metallic phases that were either produced by mechanical alloying or purchased in powder form. So, this work was divided into two parts: characterization of the metallic powders produced by mechanical alloying and characterization of the sintered cermets.

2.1. Production and Characterization of Cu–Ni and Ag–Ni Metallic Powders

Cu–Ni and Ag–Ni powders were prepared by mechanical alloying from Cu, Ag, and Ni powders. For the production of the Cu–Ni powder, the proportion 50Ni/50Cu (wt %) was used and, for the Ag–Ni production, the proportion used was 97Ag/3Ni. The alloying process was undertaken in a Retsch high-energy planetary mill for 10 h at 650 rpm. A 23-mL steel vial was utilized, filled with 16 steel balls of 7.9 mm diameter, 10 g of powder, and 8 mL of ethyl alcohol. The mechanically alloyed powders and the starting Cu, Ni, and Ag powders were analyzed by scanning electron microscopy (SEM) and X-ray diffraction (XRD) with Cu K α radiation.

2.2. Production and Characterization of the Sintered Metal–Ferrite Samples

The metal–ferrite samples were produced from 98 vol % Ni_{0.9}Co_{0.1}Fe₂O₄ and 2 vol % metallic powders. The metallic powders were commercial Ag and Ag–Cu or the mechanically alloyed powders. The commercial powders were analyzed by SEM.

Ni_{0.9}Co_{0.1}Fe₂O₄ was produced by the ceramic method, with NiO, Co₃O₄, and Fe₂O₃ powders as raw materials. The oxide powders were wet-mixed in a ball mill, dried in an oven, calcined at 900 °C for 4 h, and wet-milled again. The grinding media utilized in the ferrite production were made from alumina.

The metallic powders were added to the calcined powder and mixing was carried out with ethyl alcohol in an eccentric mill. After mixing, the ethyl alcohol was burnt from suspension so as to rapidly dry the mixture and minimize decanting of the powders.

The metal–ferrite powders were pressed in the shape of 8-mm-diameter pellets, under 40 MPa uniaxial pressure. The compacted samples were sintered using the sintering schedules presented in Table 1. Sintering was carried out in air atmosphere, with 5 °C/min heating rate, followed by dwelling in the temperatures indicated in Table 1.

Table 1. Sintering schedules of the metal–ferrite samples with different metallic phases.

Metallic Phase	Sintering Schedules
Cu–Ni	1350 °C/30 min
Ag–Ni	1350 °C/30 min
Ag	1350 °C/3 h, 1000 °C/30 min, 1000 °C/4 h
Ag–Cu	1000 °C/30 min

The sintered cermet samples were analyzed by optical microscopy (OM) and SEM equipped with energy dispersive spectroscopy (EDS) microanalysis. The samples' surfaces observed by microscopy were previously grinded with sandpaper and polished with diamond paste.

XRD was carried out in the Ag–Ni, Ag–Cu, and Cu–Ni sintered samples because Cu and Ni are soluble in the ferrite; thus, co-sintering with these alloys is expected to affect the crystal structure of the ceramic. For comparison purposes, a sintered ferrite sample was produced and its crystal structure was evaluated by XRD. The sample was an 8-mm-diameter pellet, which was produced by uniaxial compaction of the calcined powder under 40 MPa, followed by sintering at 1350 °C for 3 h.

3. Results

3.1. Characterization of the Sintered Ferrite Sample

The XRD pattern of the sintered ferrite sample is shown in Figure 1. It matches the patterns from typical spinel ferrite ceramics, such as NiFe_2O_4 (JCPDS#44-1485).

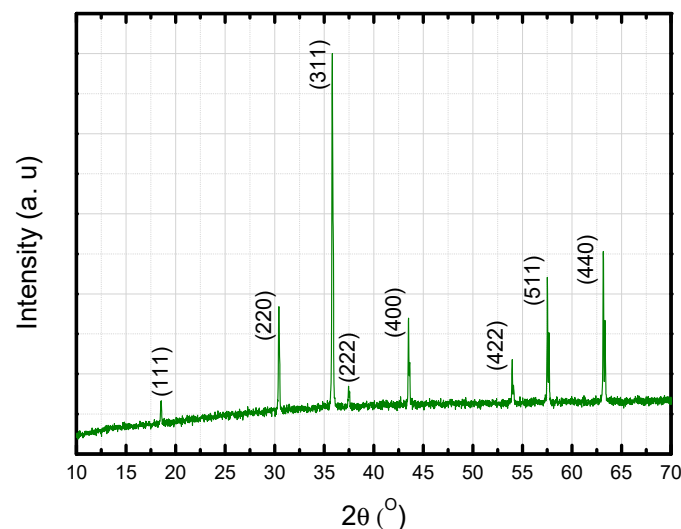


Figure 1. Diffraction pattern of the ferrite sample sintered at 1350 °C for 3 h, indicating the crystallographic planes identified in the XRD analysis.

3.2. Characterization of the Mechanically-Alloyed Ag–Ni and Cu–Ni Powders

Figures 2–7 are SEM images of the Ag, Cu, and Ni powders used in the production of the Cu–Ni and Ag–Ni alloys by mechanical alloying. The low-magnification images allow the evaluation of the particle size and morphology. The high-magnification ones allow the evaluation of the particles' microstructures. The microstructure of the particles influences the behavior of the material during milling. Porous and agglomerated particles, like the ones observed in the Ag and Ni powders, tend to break more easily.

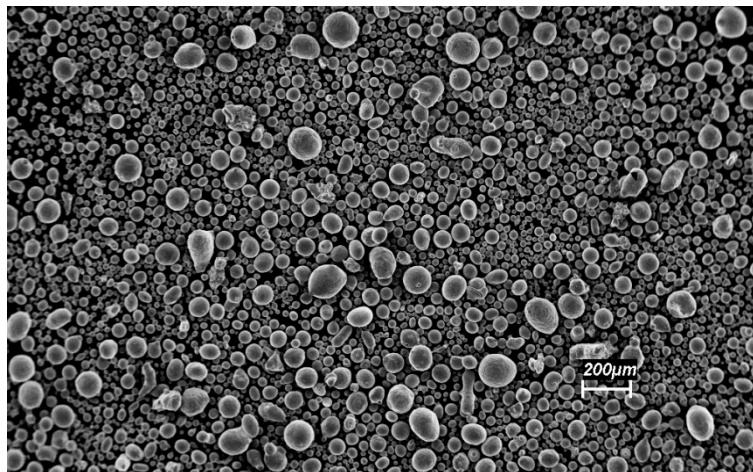


Figure 2. Low-magnification SEM image of the Cu powder.

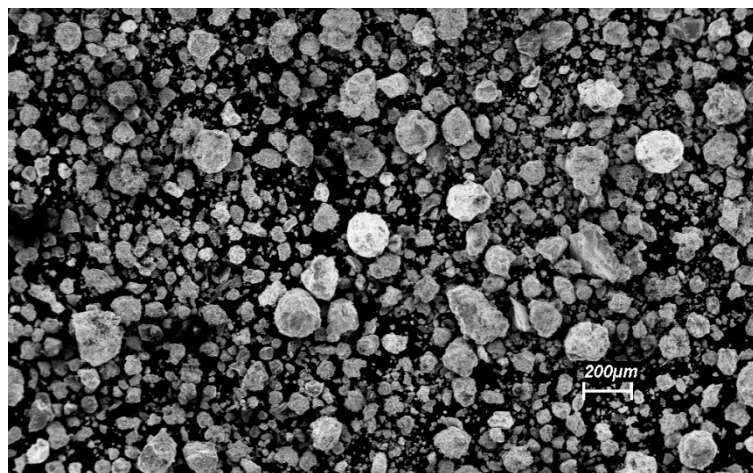


Figure 3. Low-magnification SEM image of the Ni powder.

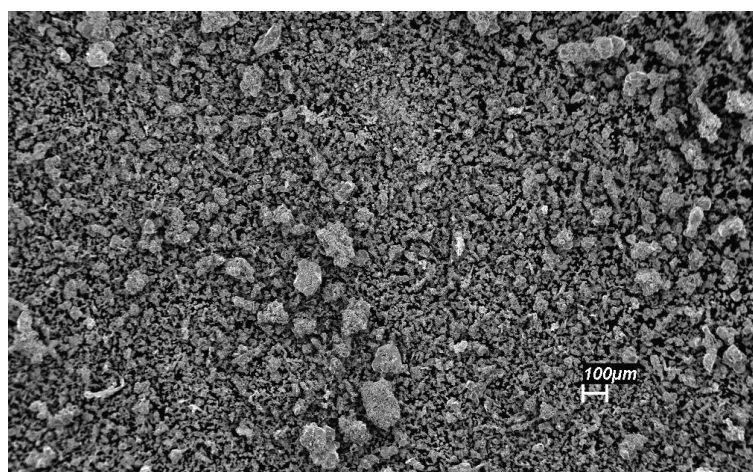


Figure 4. Low-magnification SEM image of the Ag powder.

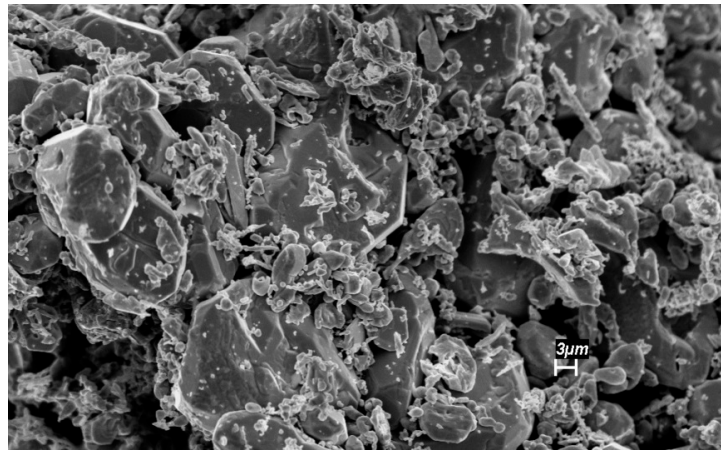


Figure 5. High-magnification SEM image of the Ag powder.

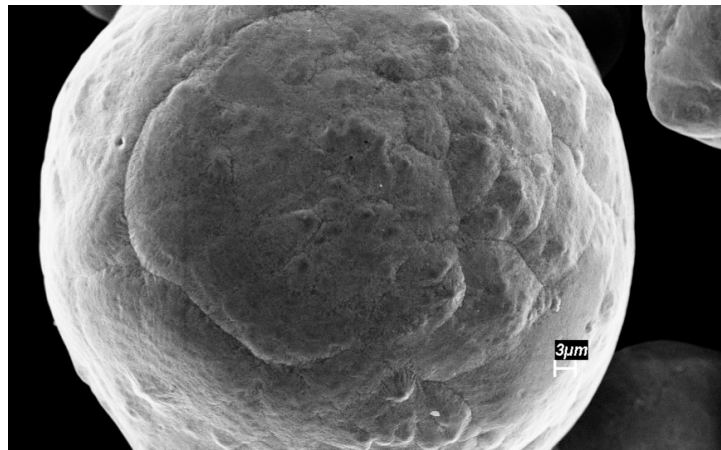


Figure 6. High-magnification SEM image of the Cu powder.

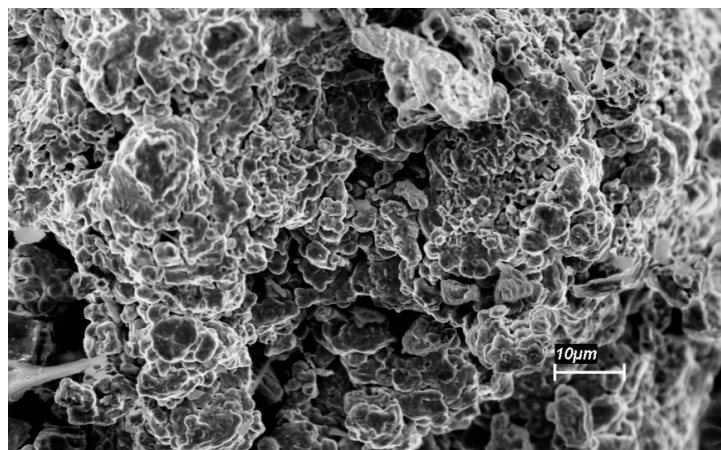


Figure 7. High-magnification SEM image of the Ni powder.

The Cu powder is composed of dense spherical particles with a large range of particle sizes (Figure 2). The particles from the Ni powder (Figure 3) have a similar size variation and the Ag powder (Figure 4) was the one with the smallest particle size.

The results from EDS chemical analysis of the powders are shown in Table 2. It is important to emphasize that the EDS analysis is semiquantitative and that the accuracy of this technique for measuring light elements, like oxygen, is low. The Ni powder presented small fractions of Fe, Mn, and Si. The presence of O in the Cu and Ni powders indicates oxidation. No elements other than Ag were detected in the Ag powder. The Ni content in the Ni powder was around 84 wt % and the Cu content of the Cu powder was around 86 wt %.

Table 2. EDS chemical analysis (wt %, 0.37 mm² area) of the raw materials used in the production of the alloys.

Raw Material	Cu	Ni	Fe	O	Mn	Si	Ag
Ni	-	84.41	2.10	10.36	1.46	1.67	-
Cu	86.54	-	-	13.46	-	-	-
Ag	-	-	-	-	-	-	100

During mechanical alloying, the metallic particles undergo plastic deformation and are repeatedly cold-welded and broken [26,27]. The plastic deformation may create coarse and flat particles such as the ones seen in Figures 8 and 9. The Ag–Ni flat particles seem thinner than the ones from the Cu–Ni, probably because of the difference in ductility of the powders processed.

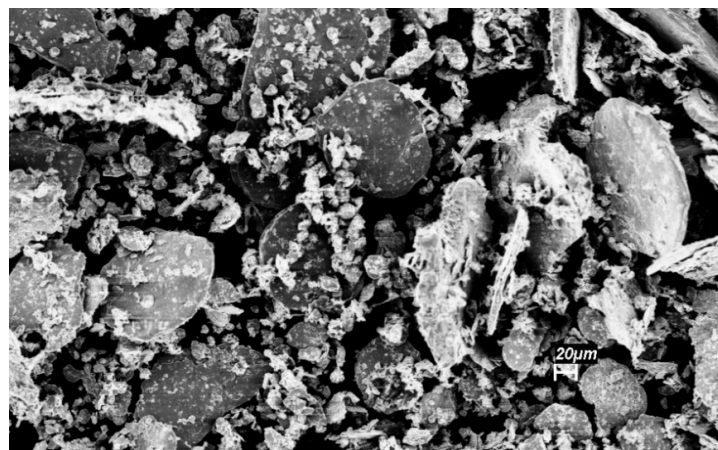


Figure 8. SEM image of the Cu–Ni powder (secondary electrons).

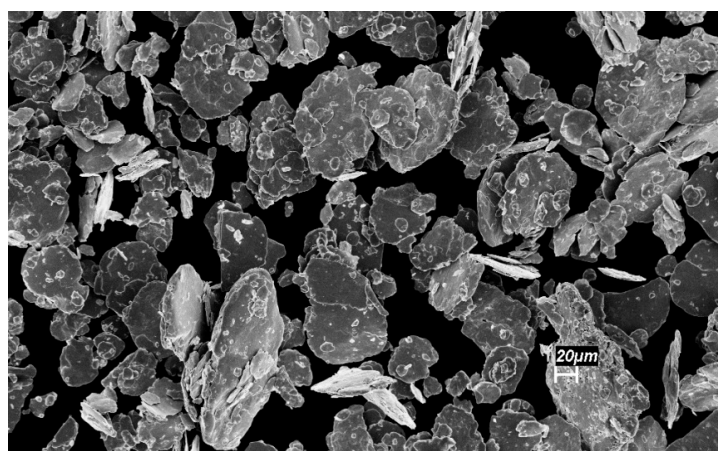


Figure 9. SEM image of the Ag–Ni powder (secondary electrons).

Figures 10 and 11 show the X-ray diffraction patterns of the mechanically alloyed metallic powders. The X-ray diffraction pattern of the Cu–Ni powder presented Cu_2O peaks, indicating oxidation of Cu.

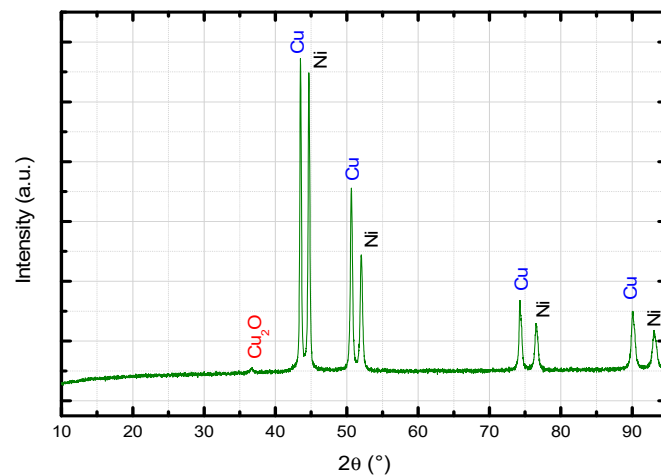


Figure 10. X-ray diffraction pattern of the Cu–Ni mechanically alloyed powder, indicating the peaks from Ni (JCPDS##04-0850), Cu (JCPDS#04-0836), and Cu_2O (JCPDS#77-0199).

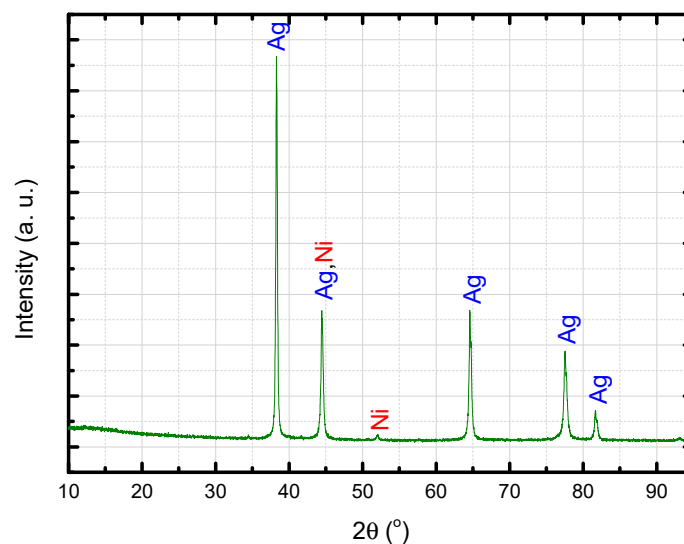


Figure 11. X-ray diffraction pattern of the Ag–Ni mechanically alloyed powder, indicating the peaks from Ag (JCPDS#87-0718) and Ni (JCPDS#04-0850).

Figures 12 and 13 show the EDS area analysis of the Ag–Ni and Ag–Cu powders. The iron detected in the Cu–Ni alloy may have originated not only from the Ni raw material, but also from the steel grinding media used in the mechanical alloying process.

The mass proportion of Fe:Ni:Cu of the Cu–Ni powder was estimated at 1.7:59.3:39.0, with a Cu:Ni proportion of 60:40, approximately. For a Cu–Ni alloy with such Cu:Ni proportion, melting of the alloy begins at 1290 °C and it is totally liquid at 1350 °C, approximately [28], but the melting point of the alloy may be affected by the iron content.

The Ag:Ni mass proportion of the Ag–Ni alloy was around 96% Ag:4% Ni. According to the Ag–Ni phase diagram [29], the 96Ag4Ni alloy melts at 1435 °C, forming a biphasic liquid. In the Ag-rich portion of the diagram [29], one can observe that very small composition variation leads to a substantial variation in melting point. In the case where the mechanical alloying process led to a

heterogeneous chemical composition of the alloy, it is possible that sintering at 1350 °C occurred in the presence of both solid and liquid metallic particles, depending on the local composition.

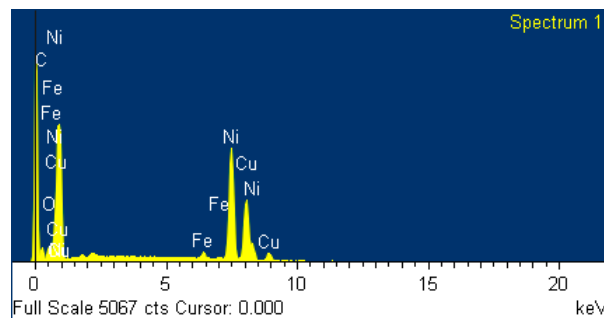


Figure 12. EDS area spectrum of the Cu–Ni alloy.

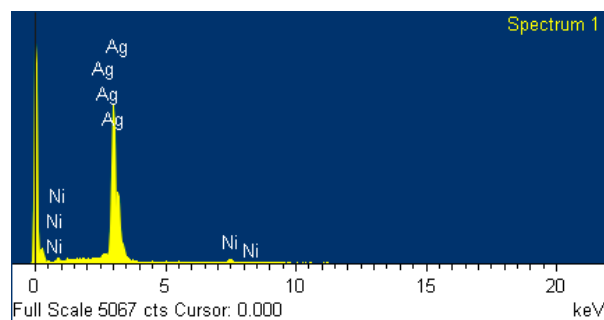


Figure 13. EDS area spectrum of the Ag–Ni alloy.

3.3. Ag–Ni Cermet

Figure 14 shows the microstructure of the Ag–Ni cermet, in which the metallic phase appears as white particles. Fragments of the largest metallic particles seem to have been removed during the polishing process. The metal–ceramic interfaces show good integrity, with the absence of cracks.

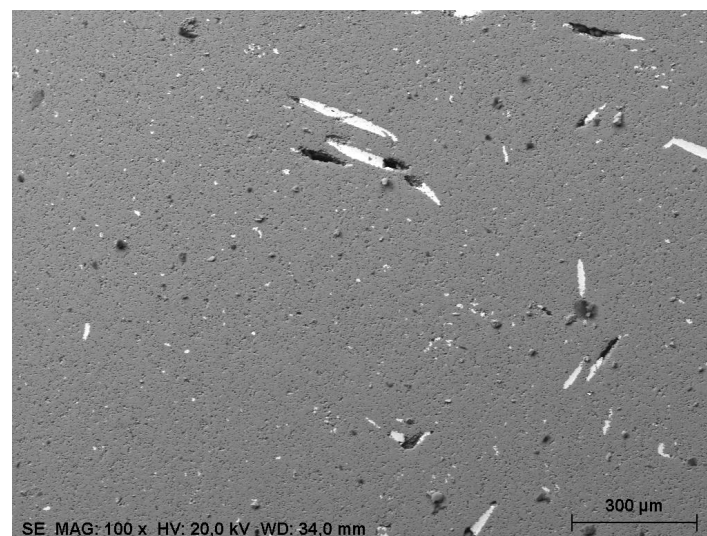


Figure 14. Microstructure of the Ag–Ni cermet.

The X-ray diffraction pattern of the sintered sample is represented in Figure 15, where the patterns observed are from the spinel ferrite and from the Ag phase (JCPDS#87-0718).

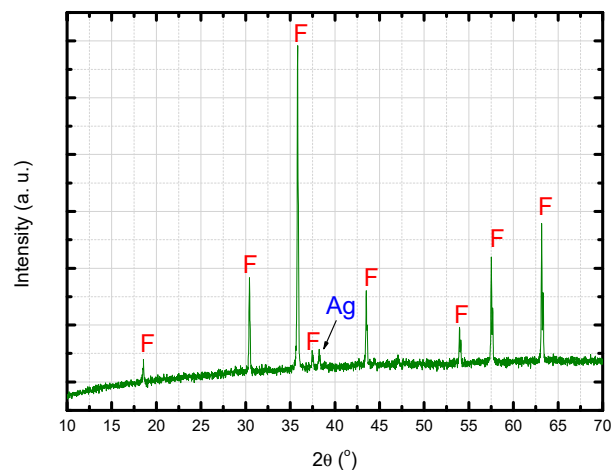


Figure 15. X-ray diffraction pattern of the sintered Ag–Ni cermet, indicating the peaks from the ferrite (F) and from the Ag phase.

From the SEM/EDS image presented in Figure 16, one can estimate that the composition of the metallic particle is 100% Ag. The supposed absence of Ni in the metallic phase indicates that it reacted with the ferrite phase.

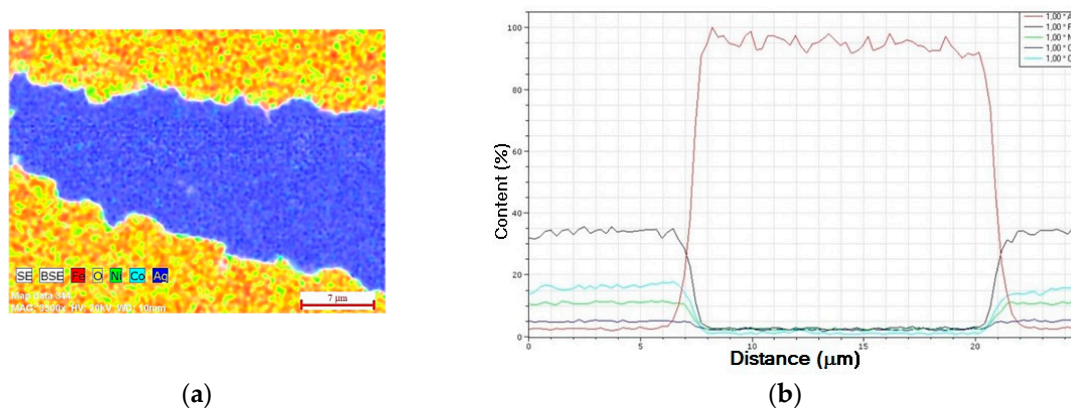


Figure 16. EDS analysis of a large metallic particle in the sintered Ag–Ni cermet. (a) 2D analysis. (b) Linescan across the particle.

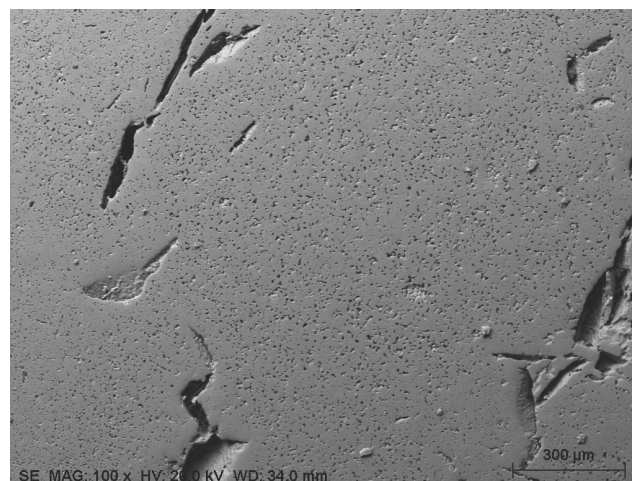
The chemical composition estimated by SEM/EDS in a small area of the sample (Table 3) indicates that the Fe:Ni:Co proportion of the cermet sample is the same as the pure ferrite: 2.1:0.8:0.1. The reason why the Ni fraction detected in the cermet is not larger than the fraction detected in the pure ferrite is that the Ni fraction in the Ag–Ni alloy is too low to cause an increase detectable by EDS. Aluminium was detected in the analysis because the ferrite was processed with alumina milling media, which caused contamination of the ferrite powder.

Table 3. Chemical composition of the Ag–Ni cermet, estimated from EDS analysis in a 338.11 μm \times 253.58 μm area.

Element	Expected	Ag–Ni Cermet	Pure Ferrite Sample [30]
Fe	28.22	34.79 \pm 0.85	36.63 \pm 0.95
Ni	12.76	13.29 \pm 0.36	13.73 \pm 0.44
O	56.43	48.42 \pm 5.95	48.49 \pm 7.58
Co	1.41	1.59 \pm 0.07	1.64 \pm 0.11
Ag	1.18	0.44 \pm 0.03	—
Al	—	1.47 \pm 0.12	1.52 \pm 0.15

3.4. Cu–Ni Cermet

According to Figure 17, no metallic particles were observed in the microstructure on the surface of the sintered Cu–Ni cermet sample. Instead, large voids were observed in regions that probably were occupied by the metallic phase before sintering or that were created by cracking of the ceramic during sintering. The EDS area analysis (Table 4) showed Cu in the composition of the material, which indicates that the alloy was incorporated by the ferrite. The Fe:Ni:Co proportion was 2.1:0.8:0.1, the same as the Ag–Ni cermet and the pure ferrite. The EDS point analysis made inside a void did not indicate a higher Ni or Cu concentration and the Fe:Ni:Co:Cu proportion found was similar to the proportion obtained in the area analysis.

**Figure 17.** Microstructure of the Cu–Ni cermet (SEM) at the surface.**Table 4.** Chemical composition (at %) of the sintered Cu–Ni cermet sample, measured by EDS.

Element	Area Analysis (338.11 μm \times 253.58 μm)	Point Analysis Inside a Void
Fe	33.88 \pm 0.86	30.36 \pm 0.25
Ni	13.82 \pm 0.08	12.37 \pm 0.58
O	47.93 \pm 6.07	52.87 \pm 3.04
Co	1.48 \pm 0.07	1.28 \pm 0.11
Cu	1.28 \pm 0.07	1.21 \pm 0.12
Al	1.61 \pm 0.12	1.89 \pm 0.11

An SEM/EDS image obtained in a transversal section of the Cu–Ni cermet (Figure 18) showed the presence of a Ni-rich region, which is probably a Ni–Cu particle.

The Cu–Ni phase diagram is isomorphous, with liquidus temperatures varying from 1083 $^{\circ}\text{C}$ (100% Cu) to 1455 $^{\circ}\text{C}$ (100% Ni) [28]. If the mechanical alloying process is not efficient in producing

a metallic powder with homogeneous composition, Ni-rich particles may remain in the powder. The melting point of these Ni-rich particles is higher than the particles with lower Ni content. Thus, the melting point of some particles may be higher than the sintering temperature. When this happens, part of the metal melts during sintering and part of it remains solid.

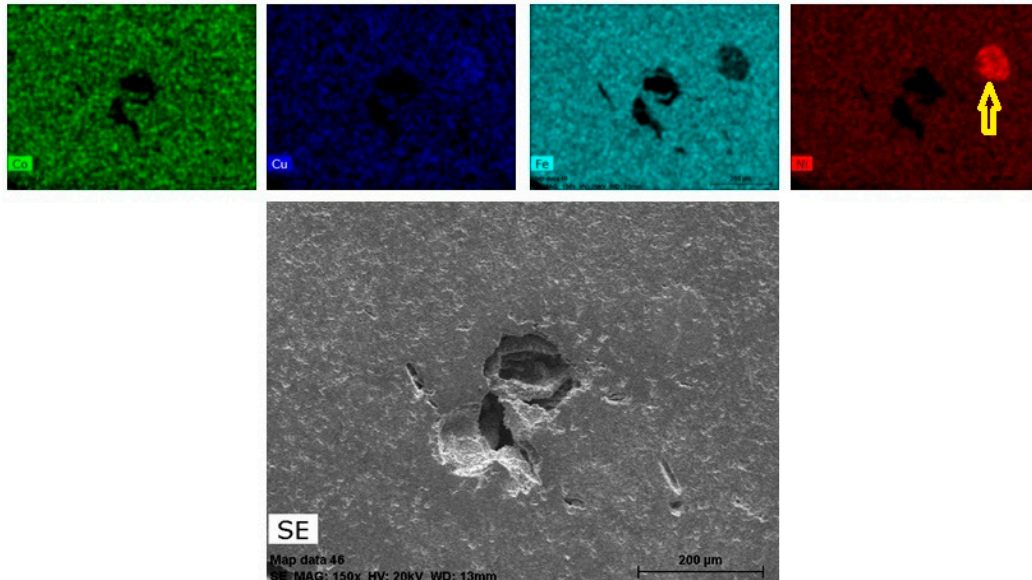


Figure 18. Microstructure of a transversal section of the Cu–Ni cermet. The EDS analysis showed the presence of local chemical heterogeneity (see the yellow arrow).

The X-ray diffraction pattern of the Cu–Ni cermet sample (Figure 19) showed only a spinel phase (ferrite). There are some possible reasons for the absence of traces of second phases in the diffraction pattern:

- second phases are present but in very low fractions, below the detection limit of the equipment;
- second phases have spinel structure, with lattice parameters similar to the ferrite matrix. In this case, the diffraction pattern of the second phase is very similar to the pattern of the ferrite matrix;
- the metallic phase totally diffused to the ferrite matrix, without precipitation of second phases (this hypothesis may be refuted according to the results presented in Figure 18).

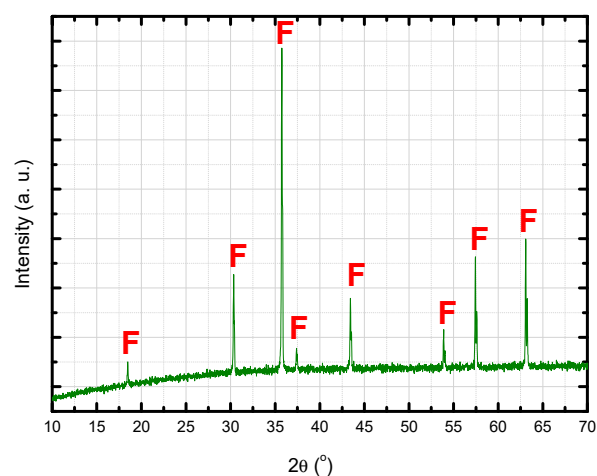


Figure 19. X-ray diffraction pattern of the sintered Cu–Ni cermet, indicating the peaks from the spinel ferrite phase (F).

3.5. Ag–Cu Cermet

Figure 20 is an SEM image of the Ag–Cu powder, where particles larger than 100 μm are present. The EDS analysis indicates an Ag:Cu mass proportion of 33.7 Cu:66.3 Ag, approximately. According to the Ag–Cu phase diagram [28], liquid phase starts forming at the eutectic temperature (779 $^{\circ}\text{C}$) and the liquidus temperature of the alloy with 33.7% Cu is just below 800 $^{\circ}\text{C}$. Thus, it is supposed that the metallic phase fully melted during the sintering of the cermet.

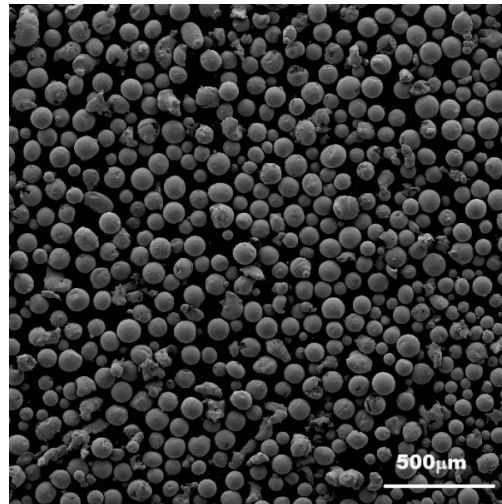


Figure 20. SEM image of the Ag–Cu powder.

The SEM image of the Ag–Cu cermet (Figure 21) shows cracks in the ceramic phase, starting from the edges of the largest metallic particles. The metal–ceramic interfaces in the smallest metallic particles are fairly sound, with no cracks around them. As seen in Figure 21b, metallic particles with sizes varying from 5 to 12 μm did not present cracks at the interfaces. Also, the round shape of the metallic particles of the Ag–Cu powder have the benefit of producing fewer stress concentration sites than powders with sharp particles.

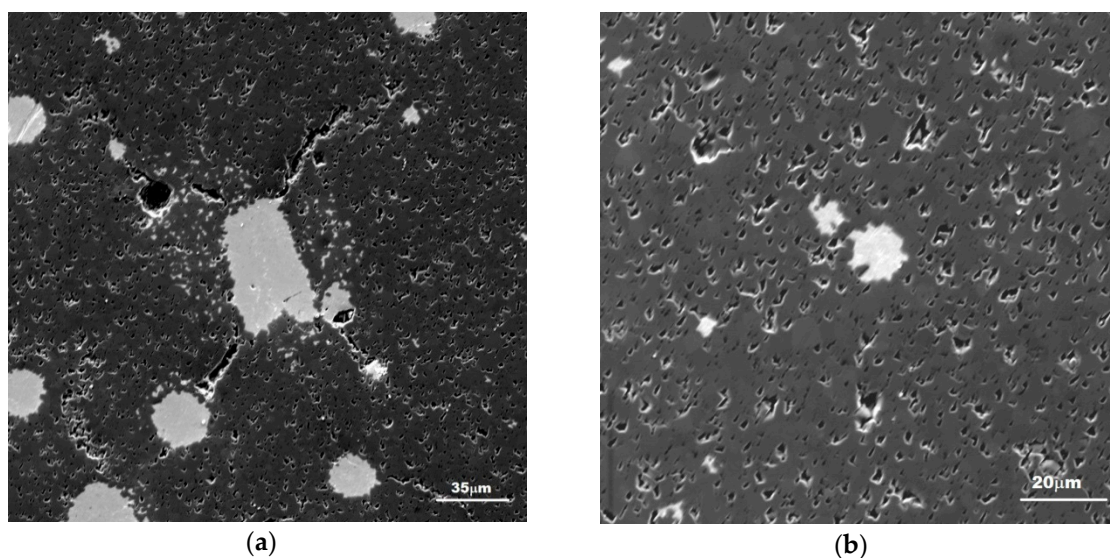


Figure 21. Microstructure of the Ag–Cu sintered sample (SEM): (a) Cracks around large metallic particles; (b) Smallest metallic particles with sound metal–ceramic interfaces.

Figure 22 presents the results from an EDS/linescan analysis across a metallic particle in the cermet. The results indicate that Cu is uniformly distributed through the sample and that the chemical composition of the metallic particle is predominantly Ag. Only some small Cu spikes are observed in the EDS spectrum from the central part of the particle (Figure 22).

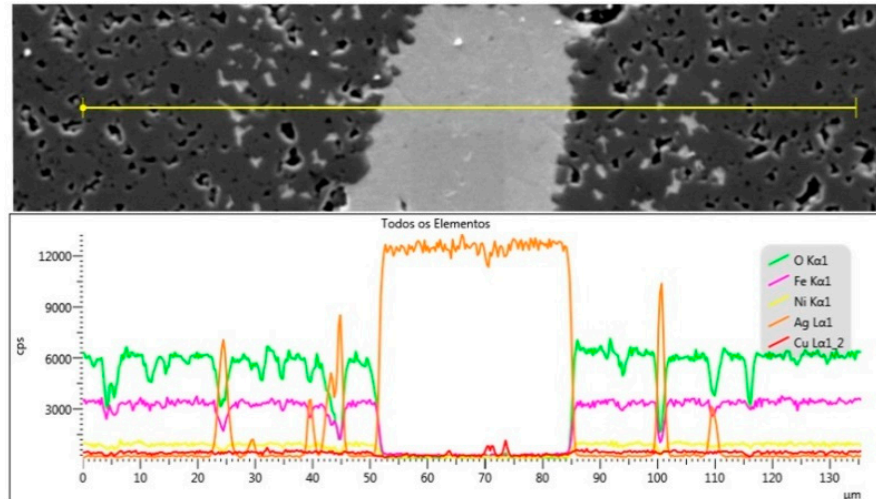


Figure 22. EDS linescan across a metallic particle observed in the microstructure of the Ag–Cu sintered sample.

Figure 23 shows the XRD diffraction pattern of the Ag–Cu sintered cermet. Peaks from Ag and from the ferrite spinel phase are present.

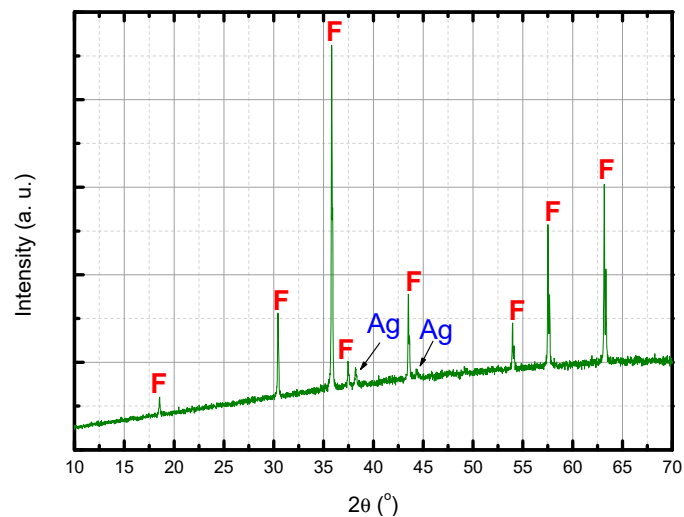


Figure 23. XRD pattern of the Cu–Ni cermet, indicating the peaks from the ferrite matrix (F) and from the metallic phase (Ag).

3.6. Ag Cermet

Figure 24 shows an SEM image of the Ag powder. Particles smaller than 4 μm are observed, as well as agglomerates with sizes around 40 μm .

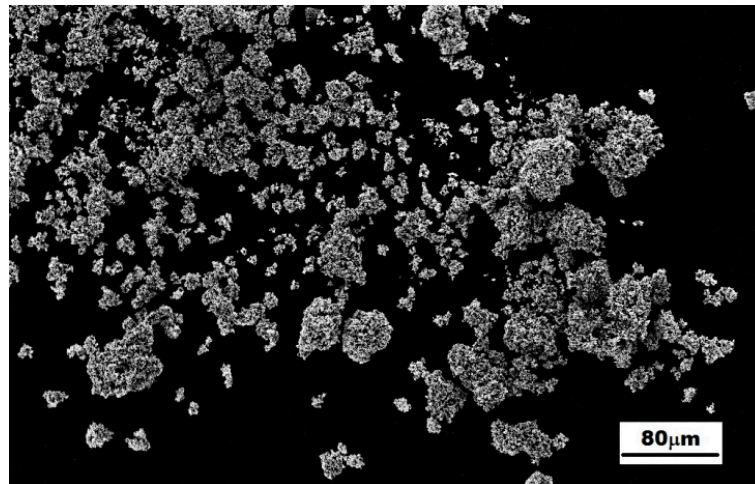


Figure 24. SEM image of the Ag powder used in the fabrication of the Ag cermet.

Figure 25 shows the microstructure of some sintered Ag cermet samples (transversal section). The sample sintered at 1350 °C for 3 h (Figure 25a) had an Ag-free layer under its surface, probably caused by the evaporation of Ag [31]. Lowering the sintering temperature to 1000 °C and shortening the sintering time to 30 min eliminated the Ag-free layer (Figure 25b) but densification did not occur. Increasing the sintering time to 4 h at 1000 °C resulted in a sample with a density of 3.29 g/cm³, which is only 64% of the theoretical density of Ni_{0.9}Co_{0.1}Fe₂O₄ [30].

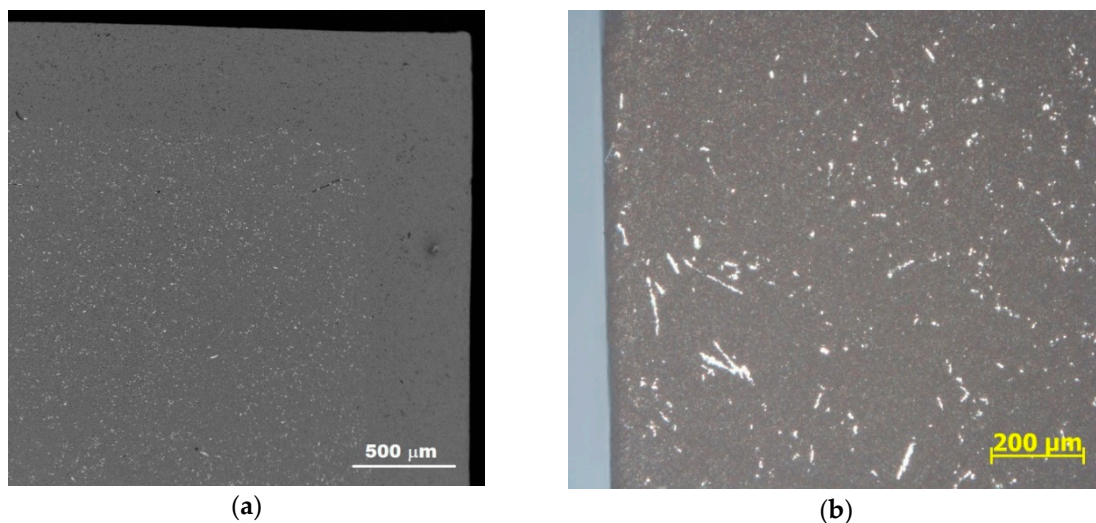


Figure 25. Microstructure of transversal section of Ag cermet samples, showing their borders. (a) Sintered at 1350 °C for 3 h (SEM). (b) Sintered at 1000 °C for 30 min (OM).

The microstructure shown in Figure 25a was observed with a higher magnification in the region where the metallic particles were present and the image obtained is shown on Figure 26. The sizes of the largest particles observed in this region were around 13 μm and the metal/ceramic interfaces had no cracks. The voids observed in the sample are derived from porosity and probably from grains that were removed from the microstructure during the grinding/polishing process.

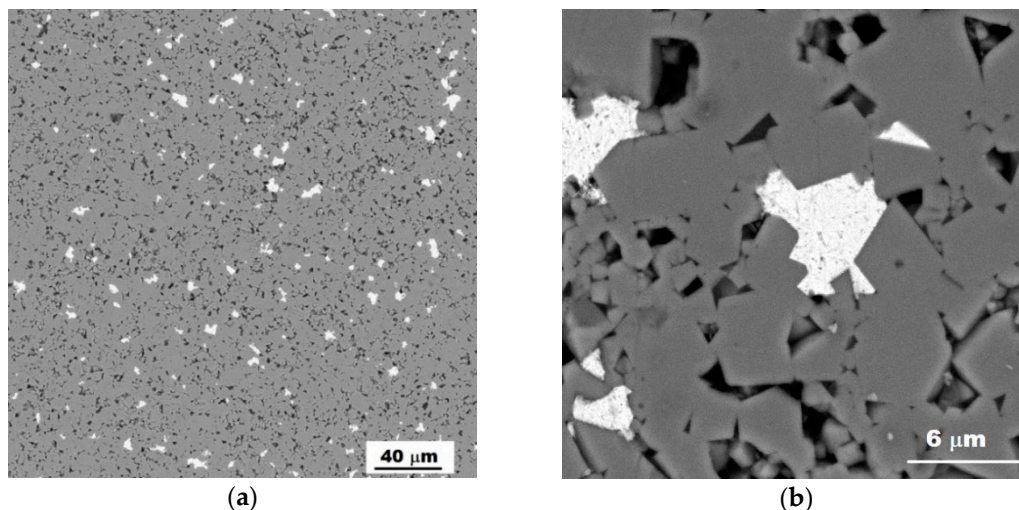


Figure 26. SEM images from the center of the transversal section of the Ag cermet sintered at 1350 °C/3 h: (a) Low magnification. (b) High magnification.

4. Discussion

According to Wachtman [32], the increase of the mechanical strength of the ceramic by means of the cermet technology is attained by the mechanism of “crack tip shielding by crack bridging”, with “second-phase ductile ligament bridging”. Particulate cermets may be produced by adding a metallic phase that, if molten during sintering of the ceramic, wets the ceramic phase and promotes liquid-phase sintering, favoring the formation of a material with lower porosity. In order to successfully produce a cermet with adequate microstructure, many processing and sintering parameters must be carefully adjusted, as has been illustrated in the experimental results presented here.

In case the metallic phase is an alloy, if its melting point varies too much with small composition variation, the chemical homogeneity of the metallic phase is of great importance. For example, Ag–Ni alloys have considerable variations in melting point with only a slight variation in Ni content. When melting of the metal phase is desired, the use of a sintering temperature that exceeds the highest melting point indicated in the alloy phase diagram may be a first alternative. However, since low porosity and high density are frequently required, the sintering temperature must not be excessively high; otherwise, it would favor grain coarsening and increased porosity. The use of dilatometry experiments to verify the densification dynamics of the material may be very useful in the task of defining the sintering thermal cycle of the cermet. For example, dilatometry is a tool for estimation of the temperature at which the second stage of sintering of the ceramic ends and the grain coarsening phenomenon occur instead of densification [33].

The results from the Cu–Ni cermet showed that the reactivity between the metallic and the ceramic phases must be taken into consideration when selecting the composition of the cermet and its production method. Although it is expected that Cu and Ni react with ferrites, the production of a ferrite-based cermet with Cu–Ni is feasible, as has been shown in the literature. A number of methods to produce ferrite/Cu–Ni cermets have been proposed, aiming for the production of inert anodes, and these cermets are usually produced from a mixture of (NiFe₂O₄ + NiO) plus a Ni or Cu metallic phase. After sintering this mixture, the microstructure is constituted of metallic particles surrounded by non-stoichiometric Ni-ferrite and nickel oxide [25]. Tailhades et al. proposed a different production route for this kind of ferrite-based cermet, in which the Cu metallic phase is partly or totally formed by reduction of metallic oxides present in the sample [10].

Although a high reactivity between the metallic and the ceramic phase may sometimes be a problem, it is desirable that the metallic phase is somewhat soluble in the ceramic matrix. This enhances the wettability of the liquid metal during sintering and facilitates the spreading of the metallic

phase among the ceramic particles. Also, small and disperse metallic particles makes spreading of the liquid metal easier during sintering. On the other hand, low wettability makes the liquid metal flow rapidly through the pores of the ceramic and form clusters.

The largest acceptable particle size of the metallic powder must be defined for each case. This issue was illustrated in the Ag–Cu cermet experiment, in which the presence of metallic particles larger than a certain size caused cracking of the ceramic phase. The stress developed during sintering by the presence of a melting metallic particle is related to its size and melting point. In the first stage of sintering, the porosity of the ceramic is interconnected, which facilitates the liquid accommodation. However, if the metallic phase melts at a temperature in which the ceramic is in the intermediate or final sintering stages, the porosity is closed and the liquid becomes confined, increasing the stress. In this point of view, the choice of a metallic phase that has a small particle size, and melts during the initial sintering stage of the ceramic, seems a good choice. The temperatures corresponding to each sintering stage of the ceramic may be estimated by dilatometry. However, changes in the chemical composition of the ceramic may occur when sintering in the presence of the metal phase and it may influence the sintering kinetics of the ceramic. The sintering kinetics and the final microstructure of the cermet thus depend on a complex interplay between several parameters. It is important to notice that even if the metal is uniformly distributed in the cermet and the microstructure is free of cracks, residual porosity reduces the mechanical strength of the ceramic. Thus, the metallic phase must be inserted in the ceramic so that its porosity is not increased in this process.

The results from this work indicate that some Ag-based alloys have potential application in ferrite particulate cermets. In the Ag and Ag–Ni cermets, the metal–ceramic interfaces were flawless. The same trend was observed in the Ag–Cu cermet, but only in the case of metal particles around 12 μm or smaller. In both Ag–Cu and Ag–Ni cermets, the compositions of the metallic particles were nearly 100% Ag after sintering, evidencing reactivity with the ferrite at high temperatures. Since the reaction between both phases may change the ferrite composition and affect its properties, precautions must be taken in order to minimize the impact of the compositional change of the ceramic phase. For example, in the production of a Ni-based ferrite cermet, the Ag–Ni alloy is expected to have less effect than the Ag–Cu alloy in changing the composition of the ferrite.

5. Conclusions

The production of ceramic-matrix particulate ferrite cermets with uniform dispersion of the metallic phase and increased mechanical properties depends on the judicious selection of several production parameters. The results from this work indicated that the following points are of great importance for cermet processing:

- appropriate choice of the chemical composition of the metallic phase, in order to minimize the change in the composition of the ferrite and to obtain adequate melting point and wettability of the metal. It is suggested to use a metallic phase with melting point within the temperature range of the first sintering stage of the ferrite;
- selection of metallic powders with small and homogeneous particle size, in order to prevent high stresses during sintering, when the metal melts.

The results from this work also indicated that the Ag–Cu and Ag–Ni alloys will probably produce ferrite particulate cermets with adequate microstructure, provided that the particle size of the alloy is around 12 μm or smaller. In the case of a Ni–Co ferrite matrix, the Ag–Ni alloy seems more appropriate because the Cu present in the Ag–Cu alloy may cause a significant change in the composition of the ferrite.

Author Contributions: Conceptualization, V.L.O.d.B.; methodology, V.L.O.d.B.; formal analysis, V.L.O.d.B. and M.S.H.; investigation, V.L.O.d.B., M.S.H., J.A.N.F., E.d.O.S.J., and J.P.B.M.; resources, V.L.O.d.B. and J.P.B.M.; writing—original draft preparation, V.L.O.d.B. and M.S.H.; writing—review and editing, V.L.O.d.B. and M.S.H.; visualization, V.L.O.d.B. and M.S.H.; supervision, V.L.O.d.B.; project administration, V.L.O.d.B.; funding acquisition, V.L.O.d.B.

Funding: This research was funded by CNPq, by means of grant number 461334/2014-3 and PIBIC/IEAv; the research also received resources from CAPES (Pró-Estratégia and scholarship at Instituto Tecnológico de Aeronáutica).

Acknowledgments: The authors acknowledge the support received from the Materials Division of the Institute for Aeronautics and Space (São José dos Campos, Brazil) and from the Photonics Division of IEAv (São José dos Campos–Brazil).

Conflicts of Interest: The authors declare no conflict of interest. The funders had no role in the design of the study; in the collection, analyses, or interpretation of data; in the writing of the manuscript, or in the decision to publish the results.

References

1. Travitzky, N. Processing of ceramic-metal composites. *Adv. Appl. Ceram.* **2010**, *111*, 286–300. [[CrossRef](#)]
2. Kim, Y.H.; Hashi, S.; Ishiyama, K.; Arai, K.I.; Inoue, M. Remote temperature sensing system using reverberated magnetic flux. *IEEE Trans. Magn.* **2000**, *35*, 3643–3645. [[CrossRef](#)]
3. De Brito, V.L.O.; Migliano, A.C.C.; Lemos, L.V.; de Melo, F.C.L. Ceramic processing route and characterization of a Ni-Zn ferrite for application in a pulsed-current monitor. *Prog. Electromagn. Res.* **2009**, *91*, 303–318. [[CrossRef](#)]
4. Bichurin, M.I.; Petrov, V.; Petrov, R.; Kiliba, Y.V.; Bukashev, F.; Smirnov, A.Y.; Eliseev, D.N. Magnetolectric sensor of magnetic field. *Ferroelectrics* **2002**, *1*, 199–202. [[CrossRef](#)]
5. Bergs, R.; Islam, R.A.; Vickers, M.; Stephanou, H.; Priya, S. Magnetic field anomaly detector using magnetolectric composites. *J. Appl. Phys.* **2007**, *101*, 024108. [[CrossRef](#)]
6. Stucki, F.F. Ferrimagnetic pressure transducer. Patent Office of London Patent 1.168.861, 29 October 1969.
7. Somaiah, N.; Jayaraman, T.V.; Joy, P.A.; Das, D. Magnetic and magnetoelastic properties of Zn-doped cobalt-ferrites-CoFe_{2-x}Zn_xO₄ (x=0, 0.1, 0.2, and 0.3). *J. Magn. Magn. Mater.* **2012**, *324*, 2286–2291. [[CrossRef](#)]
8. De Brito, V.L.O.; Cunha, S.A.; Lemos, L.V.; Bormio-Nunes, C. Magnetic properties of liquid-phase sintered CoFe₂O₄ for application in magnetoelastic and magnetolectric transducers. *Sensors* **2012**, *12*, 10086–10096. [[CrossRef](#)] [[PubMed](#)]
9. Ray, S.; Rapp, R.A. Composition Suitable for Use as Inert Electrode Having Good Electrical Conductivity and Mechanical Properties. U.S. Patent 4,454,015, 12 June 1984.
10. Tailhades, T.; Rousset, A.; Gabriel, A.; Laurent, V.; Baco-Carles, V.; Lamaze, A. Inert anode for the production of aluminium by fused bath electrolysis and method of making this anode. U.S. Patent US2007/0056848 A1, 15 March 2007.
11. De Brito, V.L.O.; Cunha, S.A.; Araújo, F.F.; Machado, J.P.B.; Bormio-nunes, C.; Silva, M.R. Processing and characterization of a Ni-Co ferrite for sensor applications. *Cerâmica* **2015**, *61*, 341–349. [[CrossRef](#)]
12. Sedlar, M.; Matejec, V.; Paulicka, I. Optical fibre magnetic field sensor using ceramic magnetostrictive jackets. *Sens. Actuators A* **2000**, *84*, 297–302. [[CrossRef](#)]
13. Chen, Y.; Jiles, D.C. The magnetomechanical effect under torsional stress in a cobalt ferrite composite. *IEEE Trans. Magn.* **2000**, *36*, 3244–3247. [[CrossRef](#)]
14. Chen, Y.; Schwichtenberg, C.R.; Snyder, J.E.; Dennis, K.W.; McCallum, R.W.; Jiles, D.C. Metal-bonded Co-ferrite composites for magnetostrictive torque sensor applications. *IEEE Trans. Magn.* **1999**, *35*, 3652–3654. [[CrossRef](#)]
15. Choi, H.S.; Kim, K.D.; Jang, J.S. Design for reliability of ferrite for electronics materials. *Electron. Mater. Lett.* **2011**, *7*, 63–70. [[CrossRef](#)]
16. Tajima, T.; Asano, K.; Furuya, T.; Iida, S.; Ishi, Y.; Kijima, K.; Kokura, S.; Mitsunobu, S.; Takahashi, T.; Takashina, H. Bonding of a microwave-absorbing ferrite, TDK IB-004, with copper for the HOM damper of the KEK B-factory SC cavities. In Proceedings of the Sixth Workshop on RF Superconductivity, Newport News, VA, USA, 4–8 October 1993.
17. Wang, Y.; Zhang, H. Low temperature brazing of chip inductors by abnormal glow discharge plasma. *IEEE Trans. Compon. Packag. Technol.* **2006**, *29*, 350–354. [[CrossRef](#)]
18. Chojnaki, E.; Gruber, T.; Sherwood, N.; Alton, W.J. Beamline RF load development at Cornell. In Proceedings of the 1999 Particle Accelerator Conference, New York, NY, USA, 29 March–2 April 1999.
19. Jin, H.; Ma, Y.; Wang, D. Growth of lead-free welding films on ferrite substrate by magnetron sputtering. *J. Vac. Sci. Technol.* **2008**, *28*, 341–345.

20. Kajiwara, K.; Hakayama, M.; Kunito, Y.; Ikeda, Y.; Hayashi, K.; Aso, K.; Ishida, T. Analysis of metal-ferrite interface in metal-in-gap heads. *IEEE Trans. Magn.* **1990**, *26*, 2978–2982. [[CrossRef](#)]
21. Hardy, J.S.; Kim, J.Y.; Thomse, E.C.; Weil, K.S. Improved wetting of mixed ionic/electronic conductors used in electrochemical devices with ternary air braze filler metals. *J. Electrochem. Soc.* **2007**, *154*, 32–39. [[CrossRef](#)]
22. Dong, W.Z.; Lin, Q.Q.; Li, Y.T.; Huang, W. Effect of sintering pressure on hot press sintering of 17Ni/(10NiO-NiFe₂O₄) cermet. *Mater. Res. Innov.* **2014**, *18*, 510–513. [[CrossRef](#)]
23. Huchet, G.; Boussuge, M.; Maurel, V.; Roustan, H. Mechanical properties of a spinel-ferrite-based cermet: Effects of temperature and oxidation. *J. Mater. Sci.* **2013**, *48*, 3264–3271. [[CrossRef](#)]
24. Tao, Y.; Li, Z.; Zhang, D.; Xiong, H.; Zhou, K. Microstructural evolution of a nickel ferrite—Copper alloy cermet during sintering and high-temperature oxidation. *J. Am. Ceram. Soc.* **2012**, *95*, 3031–3036. [[CrossRef](#)]
25. Rioult, F.; Pijolat, M.; Valdivieso, F. High-temperature oxidation of a Cu-Ni cermet: Kinetic and microstructural study. *J. Am. Ceram. Soc.* **2006**, *89*, 996–1005. [[CrossRef](#)]
26. Suryanarayana, C. Mechanical alloying and milling. *Prog. Mater. Sci.* **2001**, *46*, 1–184. [[CrossRef](#)]
27. Benjamin, J.S.; Volin, T.E. The mechanism of mechanical alloying. *Metall. Trans.* **1974**, *5*, 1929–1934. [[CrossRef](#)]
28. Van Vlack, L.H. *Princípios de Ciência dos Materiais*; Edgard Blücher: São Paulo, Brazil, 1970; pp. 233–235.
29. American Society for Metals. *ASM Handbook: Alloy Phase Diagrams*; ASM: Materials Park, OH, USA, 1992; Volume 3.
30. Hieda, M.S. Desenvolvimento de Cermets de Ferrita Ni-Co Aplicáveis em Sensores Magnetomcânicos. Master's Dissertation, Instituto Tecnológico de Aeronáutica, São José dos Campos, Brazil, 2015.
31. Jaimeewong, P.; Ngerchuklin, P.; Khamman, O.; Dechakput, T. Sintering properties and microstructure of NiMn₂O₄-silver composites. *Ferroelectrics* **2013**, *457*, 153–158. [[CrossRef](#)]
32. Wachtman, J.B. *Mechanical Properties of Ceramics*, 1st ed.; John Wiley & Sons Inc.: New York, NY, USA, 1996.
33. Zhang, Z.; Liu, Y.; Yao, G.; Zu, G.; Wu, D.; Hao, Y. Synthesis and characterization of dense and fine nickel ferrite ceramics through two-step sintering. *Ceram. Int.* **2012**, *38*, 3343–3350. [[CrossRef](#)]



© 2019 by the authors. Licensee MDPI, Basel, Switzerland. This article is an open access article distributed under the terms and conditions of the Creative Commons Attribution (CC BY) license (<http://creativecommons.org/licenses/by/4.0/>).